Transp Porous Med (2012) 94:487–504
DOI 10.1007/s11242-011-9877-8

Relative Permeability Calculations from Two-Phase Flow Simulations Directly on Digital Images of Porous Rocks

Thomas Ramstad · Nasiru Idowu · Cyril Nardi · Pål-Eric Øren

Received: 17 November 2010 / Accepted: 8 September 2011 / Published online: 30 September 2011

Abstract We present results from a systematic study of relative permeability functions derived from two-phase lattice Boltzmann (LB) simulations on X-ray microtomography pore space images of Bentheimer and Berea sandstone. The simulations mimic both unsteady- and steady-state experiments for measuring relative permeability. For steady-state flow, we reproduce drainage and imbibition relative permeability curves that are in good agreement with available experimental steady-state data. Relative permeabilities from unsteady-state displacements are derived by explicit calculations using the Johnson, Bossler and Naumann method with input from simulated production and pressure profiles. We find that the nonwetting phase relative permeability for drainage is over-predicted compared to the steady-state data. This is due to transient dynamic effects causing viscous instabilities. Thus, the calculated unsteady-state relative permeabilities for the drainage is fundamentally different from the steady-state situation where transient effects have vanished. These effects have a larger impact on the invading nonwetting fluid than the defending wetting fluid. Unsteady-state imbibition relative permeabilities are comparable to the steady-state ones. However, the appearance of a piston-like front disguises most of the displacement and data can only be determined for a restricted range of saturations. Relative permeabilities derived from unsteady-state displacements exhibit clear rate effects, and residual saturations depend strongly on the capillary number. We conclude that the LB method can provide a versatile tool to compute multiphase flow properties from pore space images and to explore the effects of imposed flow and fluid conditions on these properties. Also, dynamic effects are properly captured by the method, giving the opportunity to examine differences between steady and unsteady-state setups.

Keywords Relative permeability · Lattice Boltzmann simulations · Steady-state · Unsteady-state · Sandstone

T. Ramstad (✉) · N. Idowu · C. Nardi · P.-E. Øren
Numerical Rocks AS, Trondheim, Norway
e-mail: thomas@numericalrocks.com

1 Introduction

Accurate estimates of relative permeability functions are necessary input to reservoir models to reliably predict fluid movement and to design and optimize oil recovery processes. Just like absolute permeability, relative permeability can vary considerably throughout the reservoir depending on the local pore structure, interactions between the fluids and rock–fluid interactions. Traditionally, relative permeabilities are determined experimentally using different measurement methods (e.g. unsteady-state, steady-state and centrifuge). These measurements are often time consuming and difficult to interpret and to perform, especially under reservoir conditions. As a result, data are often scarce and there is no easy way to account for the variation of relative permeability and residual saturations in the field due to different flow conditions, pore structures and/or wettability trends.

An alternative approach to derive transport properties of rocks, and thus enrich and augment experimental measurements, is to numerically simulate fluid transport on images of the rock microstructure. This has been made possible by significant improvements in imaging (e.g. Arns et al. 2002) and modeling (e.g. Øren and Bakke 2002) of rock microstructures and by the rapid increase in computational power. The approach has been successfully applied to predict static rock properties (Øren and Bakke 2002; Knackstedt et al. 2004; Jin et al. 2004). The extension to multiphase flow is commonly done using network modeling techniques. The predictive capabilities of network models have improved greatly with recent developments in extracting topological and geometrical equivalent pore networks from microstructure images (Lindquist et al. 1996; Øren and Bakke 2003; Jiang et al. 2007), and predictive results have been demonstrated for a number of different rocks (e.g. Øren et al. 1998, 2006; Valvatne and Blunt 2004).

Although network models have many favorable features (e.g. computational speed, infinite resolution, sharp interfaces), a number of limitations still exist. In particular, it is challenging to extract topologically and geometrically equivalent pore networks that are representative for certain classes of rocks. Another issue that arises in connection with simulations of multiphase flow in porous media is to accurately capture dynamic effects (Idowu and Blunt 2010), such as mobilization and flow of discontinuous phases (Ramstad and Hansen 2006). A way to approach these challenges is to simulate the dynamics of multiphase flow directly on rock microstructure images. However, this is a difficult task since most continuum-based computational fluid dynamics techniques cannot directly combine large and small scale physical behavior. Obviously, local pore level effects like capillary barriers strongly affect multiphase flow in porous media.

The lattice Boltzmann (LB) method is a computational technique that account for many of the difficulties mentioned above. The general LB method is a mesoscopic model—between microscopic and macroscopic. Although it has limitations related to finite resolution and relies upon a simplified collision and propagation scheme of fluid distributions, it is able to correctly reproduce macroscopic behavior and at the same time capturing local microscopic effects. The kinetic approach enables the LB method to automatically maintain fluid interfaces that do not need to be tracked. In comparison, direct continuum equation solvers for multiphase flow like the level set (Sussman et al. 1994) and the phase-field (Badalassi et al. 2003) methods rely on auxiliary algorithms to track and handle the fluid interfaces in addition to solving the macroscopic flow equations. An extensive review of these and other numerical techniques for multiphase flow can be found in Tryggvason et al. (2007).

In addition, many properties related to fluid–solid and fluid–fluid interactions can be implemented in a straight forward manner in the LB method without having to include complicated kernels. These features make the LB model uniquely suited to simulate fluid flow directly

on rock microstructure images. This has been demonstrated in several studies of both single phase flow (e.g. Jin et al. 2004; Succi et al. 1989) and multiphase flow in porous media (Pan et al. 2004; Schaap et al. 2007). However, few studies have focused on verifying LB-computed multiphase flow functions such as relative permeability for realistic rocks (Martys and Chen 1996; Ramstad et al. 2010).

Verification of computed relative permeability functions by direct comparisons with measured data are complicated by a number of factors. First of all, computations are performed on images that are orders of magnitude less than the experimental sample. Uncertainties about sample heterogeneities thus always exist. Next, in real rocks there is no easy way to a priori determine wettability or contact angle distribution at the pore level. Wettability, of course, strongly affects all measured multiphase flow functions. Finally, it is well known that experimentally determined relative permeabilities depend on the measurement method. For example, the unsteady-state displacement method is an indirect method because relative permeabilities are calculated, not measured. To compare measured and predicted relative permeabilities, the LB simulations should mimic the applied measurement method, including experimentally imposed boundary conditions (e.g. flowrate and applied pressure drop).

In this article, we report the ongoing development of LB simulations aimed at reproducing the unsteady and steady-state methods for measuring relative permeability. We first provide a brief description of the underlying dynamics of our LB method of choice. Next, we describe the implementation of the different setups and boundary conditions used to mimic the different measurement methods. Finally, we report drainage and imbibition relative permeabilities derived from LB simulations of unsteady and steady-state displacements. The simulations are performed on pore space images of water-wet Bentheimer and Berea sandstone. The computed relative permeabilities are compared with available experimental data.

2 LB Method

The general LB model is a spatially discrete approach to fluid dynamics. It involves relaxing a set of fluid particle distributions $f_i(\mathbf{x}, t)$ towards an equilibrium Boltzmann distribution f_i^{eq}. The dynamics is governed by moving and colliding particle distributions on a lattice. The fluid distributions are located in space on lattice nodes $\mathbf{x}$ at time t, and they can propagate to neighboring nodes through fixed directional links i. In this process, they collide with other fluid distributions and are subsequently redistributed according to a collision step. Reviews of the LB method can be found in textbooks (e.g. Rothmann and Zaleski 1997; Succi 2001; Sukop and Thorne 2006).

Even though the LB interaction scheme is highly simplified and contains very limited degrees of freedom, the method is able to capture microscopic effects and at the same time produce numerical solutions to macroscopic hydrodynamics. Local fluid density ρ and velocity $\mathbf{u}$ at position $\mathbf{x}$ can be derived from the distributions

$$\rho = \sum_i f_i(\mathbf{x}, t), \tag{1}$$

$$\rho \mathbf{u} = \sum_i f_i(\mathbf{x}, t)\mathbf{c}_i, \tag{2}$$

where $\mathbf{c}_i$ is the directional velocity vector for a single distribution. Macroscopic quantities like overall fluid velocity, density and pressure can be derived from these relations by summing up over the entire lattice.

The results in this article are obtained on a three-dimensional lattice with 18 velocity vectors and rest distribution $i = 0$ with $\mathbf{c}_0 = (0, 0, 0)$. This lattice type is named $D3Q19$. The form of the pseudo-equilibrium distribution $f_i^{\mathrm{eq}}(\mathbf{x}, t)$ for the $D3Q19$ lattice is defined as

$$f_i^{\mathrm{eq}} = w_i \rho \left[1 + 3\mathbf{c}_i \cdot \mathbf{u} + \frac{3}{2} \left(3(\mathbf{c}_i \cdot \mathbf{u})^2 - \mathbf{u}^2 \right) \right], \tag{3}$$

where the factor w_i is a weight factor relating to the particular directional link i, and ρ and $\mathbf{u}$ are defined in Eqs. 1 and 2. For the $D3Q19$ model, the weights are

$$w_i = \begin{cases} \frac{1}{3}, & \text{for } i = 0\,, \\ \frac{1}{18}, & \text{for } i = 1, \ldots, 6, \\ \frac{1}{36}, & \text{for } i = 7, \ldots, 18. \end{cases} \tag{4}$$

With these quantities defined, the local propagation and collision process can be summarized as follows:

$$f_i(\mathbf{x} + \mathbf{c}_i, t + 1) - f_i(\mathbf{x}, t) = \Lambda_{ij} \left(f_j - f_j^{\mathrm{eq}} \right), \tag{5}$$

where the timestep is set to one. The static scattering matrix $\mathbf{\Lambda}$ governs the relaxation of the distribution. $\mathbf{\Lambda}$ is symmetric, but can attain quite complex forms. However, it is customary to diagonalize $\mathbf{\Lambda}$ and to simplify even further by exchanging all the diagonal elements with one single relaxation parameter ω so that the relaxation process takes the form

$$f_i(\mathbf{x} + \mathbf{c}_i, t + 1) - f_i(\mathbf{x}, t) = -\omega \left[f_i(\mathbf{x}, t) - f_i^{\mathrm{eq}}(\mathbf{x}, t) \right], \tag{6}$$

where $\omega = 1/\tau$ and τ is the relaxation time towards equilibrium. This approximation is called the Bhatnagar–Gross–Krook (BGK) LB method (Bhatnagar et al. 1954). Kinematic viscosity is related to the relaxation parameter as

$$\nu = \frac{1}{6} \left(\frac{2 - \omega}{\omega} \right). \tag{7}$$

The local fluid pressure is calculated according to an ideal gas assumption $P = c_{\mathrm{s}}^2 \rho$, where the speed of sound for the $D3Q19$ lattice is $c_{\mathrm{s}} = \sqrt{1/3}$.

The LB model itself produces results that are associated with the lattice. In order to compare the output to physical systems, it has to be converted from lattice units to physical units. This rescaling is done by the use of some fundamental scaling quantities characteristic for the physical system, i.e. length, l_{p}, fluid density, ρ_{p} and time, t_{p}. The two quantities, l_{p} and ρ_{p}, are determined directly by the lattice resolution and the fluid properties. The time scale, t_{p}, has to be set, following a dimensional analysis, so that the other fluid properties are consistent (Ramstad et al. 2010; Schaap et al. 2007). For example, the physical kinematic viscosity will relate to the lattice value as $\nu_{\mathrm{phys}} = \nu(l_{\mathrm{p}}^2/t_{\mathrm{p}})$, and the physical pressure as $P_{\mathrm{phys}} = P(\rho_{\mathrm{p}} l_{\mathrm{p}}^2/t_{\mathrm{p}}^2)$.

2.1 Multiphase Flow

For multiphase flow, the fluid phases have to be treated separately. However, they co-exist on the same grid and the mass and momentum conservation of Eqs. 1 and 2 apply to the collective behavior of the phases α

$$f_i(\mathbf{x}, t) = \sum_{\alpha} f_i^{\alpha}(\mathbf{x}, t). \tag{8}$$

Immiscible fluid–fluid interaction relates to surface tension and subsequent phase separation. Several different models have been proposed to incorporate this effect (Gunstensen et al. 1991; Shan and Chen 1993; Swift et al. 1995). Which model to incorporate depends on the specific system under investigation. Whichever model is chosen, it has to obey the Laplace law for a curved surface.

In all models, the pressure difference between the phases is obtained by adding a local force perturbation to the fluid distributions. The major differences arise when the fluids are to be separated. Latva-Kokko and Rothmann (2005) presented a method that builds on the colour gradient separation by Gunstensen et al. (1991). It "de-mixes" the fluids according to a colour gradient

$$\mathbf{g} = \sum_i \mathbf{c}_i \sum_j \left(f_j^{\alpha 1}(\mathbf{x} + \mathbf{c}_i) - f_j^{\alpha 2}(\mathbf{x} + \mathbf{c}_i) \right), \tag{9}$$

where j runs over the nearest neighbors. The strength of the interaction is governed by an extra local force that is proportional to the surface tension, σ (Rothmann and Zaleski 1997). Other separation methods, like the popular one developed by Shan and Chen (1993), use a phase difference potential to include a force that automatically separates the fluids. This is a more physical approach since it includes a pseudo-potential. The drawback is that surface tension cannot be linearly controlled by a single tuning parameter, $A \propto \sigma$.

Fluid–solid interaction is easily maintained by fixing the colour gradient close to the solid so that the fluid phases feel different attraction and repulsion by the walls. The wetting angle can thus be accurately defined within the resolution of the grid. Since we are dealing with completely immiscible fluids in this article, we implement the colour gradient method for fluid–fluid and fluid–solid interaction.

In the recent years, several versions of the LB method have been used to address challenges in connection with multiphase flow simulations. Particularly, the multiple relaxation time (MRT) scheme (d'Humières et al. 2002; Ahrenholz et al. 2008)—that basically utilizes the entire scattering matrix in Eq. 5—has been applied to address anomalous behaviour of solid interface placement. This can be a problem for the BGK single relaxation time algorithm, and can affect the calculation of absolute quantities like single-phase permeability (Pan et al. 2006). In addition, the MRT algorithm has also been reported to give enhanced stability when treating very low viscosities (Lallemand and Luo 2000). On the other hand, the MRT algorithm is more time consuming and contains an increased number of control parameters.

Another issue is how to address large density contrasts. Some studies argue that the colour gradient method cannot handle such situations and that phase potential algorithms have to be used instead (e.g. Inamuro et al. 2004). However, for the fluid pairs examined in this study, with the focus on relative quantities, the BGK algorithm and the colour gradient method seem adequate.

3 Relative Permeability

The relative permeability k_r enters into the phenomenological description of multiphase flow in porous media in terms of an extension of Darcy's law. The generalized Darcy's equation for creeping flow is written as

$$\mathbf{v}_\alpha = -\frac{k_{\mathrm{r},\alpha}(S_\alpha)k}{\mu_\alpha} \nabla P_\alpha, \tag{10}$$

where α refers to the fluid phase, and S_α is the saturation. For two-phase flow, the fluid phases are categorized as either wetting or nonwetting fluid and α =w, nw. The term $\mathbf{v}_\alpha$ is the volumetric fluid velocity of phase α, also referred to as the *Darcy velocity*

$$\mathbf{v}_\alpha = \frac{Q_\alpha}{A}\mathbf{n}, \tag{11}$$

where Q_α is the flowrate of phase α, and A is the cross section of the sample with the unit vector $\mathbf{n}$ in the flow direction. We calculate $\mathbf{v}_\alpha$ by averaging the local velocities from Eq. 2 over the entire pore space,

$$\mathbf{v}_\alpha = \phi \left\langle \sum_{\mathbf{x}} \frac{\rho_\alpha}{\rho}\mathbf{u} \right\rangle, \tag{12}$$

where ϕ is the porosity of the sample.

The validity of the relative permeability concept hinges on several fundamental issues (Marle 1981; Avraam and Payatakes 1999). If the flow is dominated by capillary forces, it is assumed that the different phases flow in separate channels and that the fluids are hydrodynamically decoupled. Under such conditions, Eq. 10 is strictly valid. For a given displacement process, relative permeability then depends only on pore structure, wettability and phase saturations. This changes if viscous effects become important. Increased viscous pressure drop can lead to viscous coupling and mobilization of trapped fluids. The balance between capillary and viscous forces is given by the dimensionless capillary number normally defined as

$$Ca = \frac{\mu(Q_{\text{tot}}/A)}{\sigma}, \tag{13}$$

where Q_{tot} refers to the total flowrate of both phases, μ is the effective viscosity and σ is the surface tension. For low capillary numbers, typically $Ca < 10^{-6}$, capillary forces dominate and the assumption of decoupled phases is correct. However, if viscous effects start to influence the fluid transport, typically at $Ca > 10^{-5}$, relative permeabilities change and eventually shift towards a linear dependency with saturation in the near miscible region (Bardon and Longeron 1980).

There are two main experimental setups for measuring relative permeability: *unsteady-state* and *steady-state*. Extensive reviews of these methods can be found in Honarpour et al. (1986). We intend to transfer both setups to our LB simulations on rock microstructure images. In that context, several challenges arise in the implementation of boundary conditions and how we record the transport and transform it into relative permeability relations.

3.1 Steady-State

In a steady-state experiment, both fluids are injected simultaneously at constant and known flowrates. Steady-state is assumed when the fractional flow upstream is equal to that downstream and/or the pressure drop across the sample is constant. The stationarity of Eq. 10 is then fulfilled and relative permeability can be measured directly. However, care must be exercised to minimize capillary end effects.

To mimic steady-state experiments, we distribute fluid phases in the model according to a target saturation. Flow at a given Ca is then commenced. We impose periodic boundary conditions and allow both fluids to enter and exit the model. Phase saturations are thus constant during the simulations. We apply the same body force to each phase, thus the global pressure

drop is the same for both phases. This eliminates capillary end effects since no gradients in capillary pressure exist.

The two phases flow until the relative permeabilities and the pressure drop have converged within a criterion $\epsilon < 10^{-5}$. For a finite model, there will be local invasion bursts that disturb a monotonic convergence; therefore, the convergence is based on a least square analysis of the long-term drift in the data, less sensitive to short-term fluctuations. When the system has converged and steady-state flow is established, we obtain the two-phase $k_{r,\alpha}$ as

$$k_{r,\alpha} = \frac{v_\alpha(S_w)}{v_0} \frac{\Delta P_0}{\Delta P(S_w)}, \tag{14}$$

with single-phase quantities labeled sub-zero. Equation 14 assumes that the single phase relative permeability $k_{r,0} = 1$. To reproduce hysteretic relative permeability curves, new phase saturations are established by injecting fluid into the model according to the direction of the saturation change (i.e. decreasing or increasing S_w) and the previous steady-state fluid configuration. This ensures that saturation and fractional flow change according to the experimental flow history.

3.2 Unsteady-State

The unsteady-state method is basically a displacement process. It is widely used because it is fast and qualitatively resembles the flooding process in the field. However, it is an indirect method. Relative permeabilities are calculated, not measured. Typically, the Johnson, Bossler and Naumann (JBN) method (Johnson et al. 1959) or its variants are used to calculate relative permeabilities from measured production data and pressure drop. This method is based on the assumptions that the flow velocity is high enough—thereby making capillary end effects negligible and that the flow velocity is constant. The phases should in addition behave as immiscible and incompressible fluids comprising a stable displacement.

To set up our unsteady-state simulations, we use periodic external boundary conditions. Both fluids can exit the model, but only the displacing fluid can enter the model. This makes the velocity field continuous during the displacement and enhances the stability of the simulations. The pressure field is controlled by a body force that is applied equally to both phases. The body force is regulated to keep a constant total mean velocity and thus constant capillary number (Ramstad et al. 2010). The effluent composition and pressure drop across the model are continuously monitored. The setup of the boundary conditions is depicted in Fig. 1.

4 Results and Discussion

Digitized rock microstructure images were acquired from X-ray tomography (MCT) of Bentheimer and Berea sandstone. These rocks are well-sorted and homogeneous, and consist mainly of quartz and feldspar. Minor amounts of authigenic clay are present in both rocks. Grid and computed petrophysical data for the images are given in Table 1. The samples are water-wet and we have chosen a uniform contact angle of $\theta = 35°$ which is consistent with oil–water contact angles in water-wet rocks. The fluid properties used in the LB simulations are summarized in Table 2.

The MCT images are segmented into solid and void space only, and clay associated porosity, that contributes to the "irreducible" wetting saturation S_{wi}, is thus not captured. The experimental S_{wi} measured by the porous plate method for the Bentheimer samples is $S_{wi} = 0.05$ (Øren et al. 1998), while the experimental S_{wi} for the Berea samples is estimated

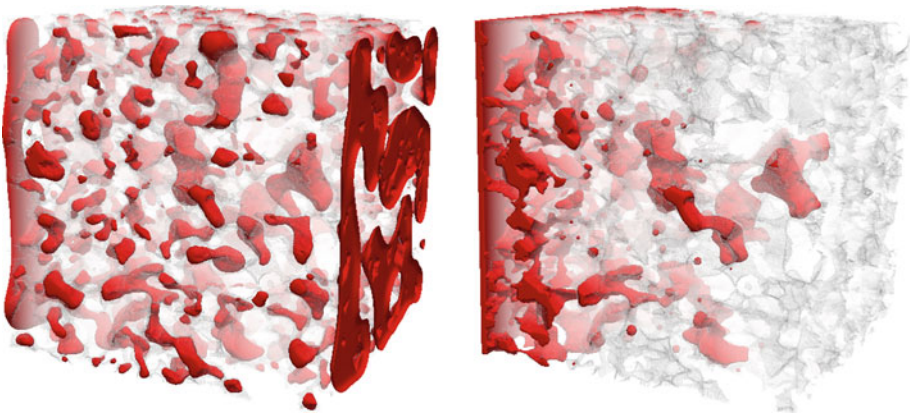

Fig. 1 X-ray microtomography image of the Bentheimer sample with snapshots of nonwetting fluid configurations (*red*) for hence periodic boundary conditions (*left*) and single phase injection (*right*). The size of the sample is approximately 8 mm^3

Table 1 Grid properties of the samples and the simulation types for which they are used

Rocktype	Size ($L_x \times L_y \times L_z$)	Resolution (μm)	k_{abs} (mD)	Porosity
Bentheimer	$256 \times 256 \times 256$	6.67	1,910	0.219
Berea	$256 \times 256 \times 256$	5.345	1,243	0.193

Table 2 Fluid parameters for the LB simulations and the experiments

Quantity	Symbol	Simulations	Experiments		Unit
		Berea/Bentheimer	Berea	Bentheimer	
Density nonwetting fluid	ρ_{nw}	900	n/a	760	kg/m^3
Density wetting fluid	ρ_w	900	n/a	1020	kg/m^3
Viscosity nonwetting fluid	μ_{nw}	1.23×10^{-3}	1.39×10^{-3}	1.4×10^{-3}	Pa s
Viscosity wetting fluid	μ_w	1.23×10^{-3}	1.05×10^{-3}	1.06×10^{-3}	Pa s
Surface tension	σ	25×10^{-3}	n/a	35×10^{-3}	N/m

to $S_{wi} = 0.2$ based on the experimental steady-state primary drainage data with reported end-point wetting saturations: $S_w = 0.244$ and $S_w = 0.28$ (Oak et al. 1990). To be consistent when comparing measured and predicted relative permeabilities for the Berea sample, we normalize experimental S_w to account for the "drainable" pore volume (PV) only (Dullien 1992), i.e.

$$S_w = \frac{S_w^* - S_{wi}}{1 - S_{wi}}, \tag{15}$$

where S_w^* is the total saturation of the wetting fluid.

The Berea sample used in the experiment had an absolute permeability of 1000 mD, and the experiment was repeated on the same sample to produce the data sets. On the other hand, three different Bentheimer samples with absolute permeabilities 2820 mD with a porosity

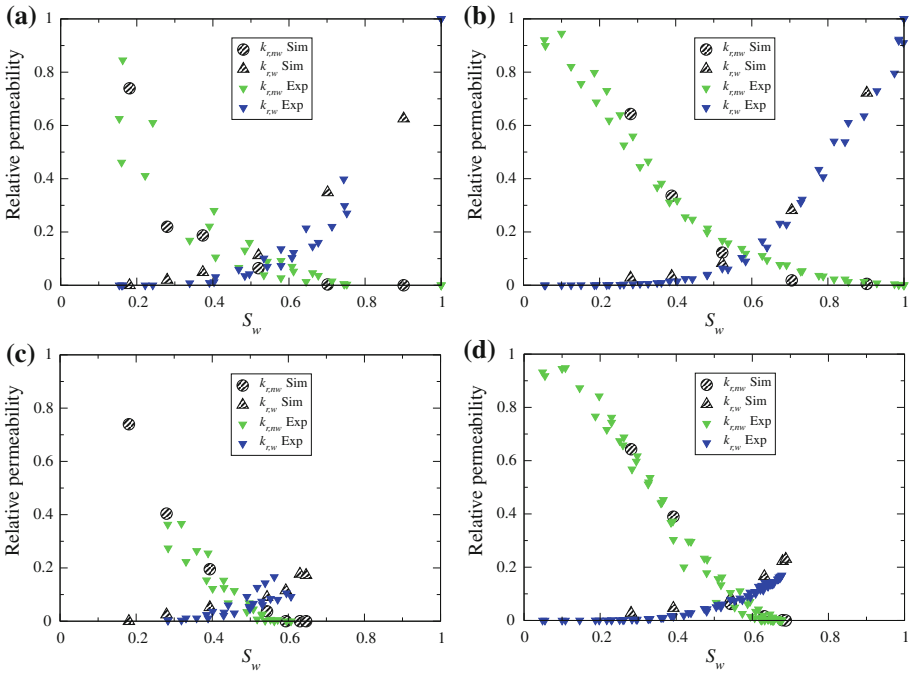

Fig. 2 Steady-state simulation results for the Bentheimer sample (*left column*) and the Berea sample (*right column*). **a** and **b** Show the drainage cycle while **c** and **d** show the imbibition cycle. All results are compared to several experimental data sets with the same flow conditions. This is to illustrate that the scattering of experimental data is taken into account

of $\phi = 0.241, 2840$ mD with a porosity of $\phi = 0.232$ and 2930 mD with a porosity of $\phi = 0.237$ were used and the experiments were carried out once. The petrophysical data for the Bentheimer samples are reasonably close, and all the three experimental data are reported. The grid and petrophysical data for the images are given in Table 1. In the following sections, we compare steady-state experimental data with both steady-state and unsteady-state simulations due to unavailability of relevant unsteady-state data.

4.1 Steady-State

Figure 2 summarizes the results from the steady-state LB simulations on the Bentheimer and Berea images. The results are compared with the experimental steady-state data (Øren et al. 1998; Oak et al. 1990), and the simulations were done at similar flow conditions and comparable fluid properties as stated in Tables 2 and 3. Hence, the choice of setup gives a good basis for direct comparison between the simulated and experimental data.

The agreement for both $k_{\mathrm{r,w}}$ and $k_{\mathrm{r,nw}}$ is fair to good for the entire range of saturations, both for drainage and imbibition, and the simulated residual nonwetting phase saturation is similar to the experimental one. There is a slight over-prediction of $k_{\mathrm{r,w}}$, but this is most likely caused by resolution effects to the wetting films making them thicker and more conductive than what would be the case in a real sample.

Calculation times for given hardware requirements are tabulated in Table 3. We have observed from the simulations that lowering the capillary number causes more fluctuations

Table 3 Runtimes and hardware requirements for the steady-state simulations

Rocktype	Simulation type	Capillary number (Ca)	CPUs	Time (h)
Bentheimer	Drainage	2.0×10^{-6}	40	≈21
Bentheimer	Imbibition	2.0×10^{-6}	40	≈21
Berea	Drainage	1.0×10^{-6}	40	≈30
Berea	Imbibition	1.0×10^{-6}	40	≈30

The CPUs are HP Xeon 2.66 Ghz quad-core processors

to the data, and thus convergence takes longer than for higher capillary numbers. However, the LB method is in general a computationally heavy method, and a single simulation has to be run in parallel on multiple computer processors (CPUs) when treating large systems.

4.2 Unsteady-state Drainage

In order to estimate the relative permeability from the JBN method, it has to be assumed that capillary pressure effects are negligible compared with viscous effects. The assumption is clearly violated at low capillary numbers similar to those shown in Table 3. Hence, for the purpose of measuring the relative permeability, we have run our unsteady-state simulations at higher Ca.

Figure 3 shows a qualitative comparison between high and low flowrate unsteady-state drainage simulations, with both snapshots of a momentary fluid configuration and the associated saturation profile of the invading fluid. For the low flowrate case (Fig. 3, right) with $Ca = 5.0 \times 10^{-6}$, it is assumed that the capillary forces are dominant. The snapshot shows a fingering front that can be categorized as capillary fingering. This kind of displacement produces a front stabilized by the capillary forces, and the first breakthrough does not occur until $S_{\mathrm{nw}} \approx 0.5$.

In the case of the high flowrate displacement carried out at $Ca = 1.0 \times 10^{-4}$ (Fig. 3, left), the viscous forces are prevalent. As a result, the stabilizing capillary forces are less pronounced, and the initial displacement is not stable. A visible fingering front of the injected fluid penetrates the system at $S_{\mathrm{nw}} \approx 0.3$. The associated saturation profile shows that there is a gradual displacement of the wetting fluid towards the outlet rather than a compact displacement. Qualitatively, this shows that viscous instabilities affect the displacement at high flowrates, and such effects may impact the calculations of the relative permeability.

Through the remaining section, we focus on the high $Ca = 1.0 \times 10^{-4}$ case where viscous forces dominate. Its production of the defending wetting fluid is shown in Fig. 4. After breakthrough of the main nonwetting front, the pressure declines slowly before it relaxes. This is mainly due to slow drainage of wetting fluid through high resistance flow paths (i.e. wetting films). We assume that the wetting phase is continuous throughout the model with a well-defined pressure drop over the model.

Figure 5 shows relative permeabilities derived by the JBN method using the simulated production and pressure profiles. We note that the endpoint S_{w} is greater than that for the steady-state results. This is due to capillary end effects. Even though the flow is categorized as viscous dominated, narrow pores exhibit relatively larger capillary barriers which require a large viscous pressure drop to be invaded. The nonwetting fluid flows only when the viscous pressure gradient exceeds the capillary pressure gradient. In the final state, both gradients are balanced. Lower endpoint S_{w} values can of course be reached by increasing the Ca of the

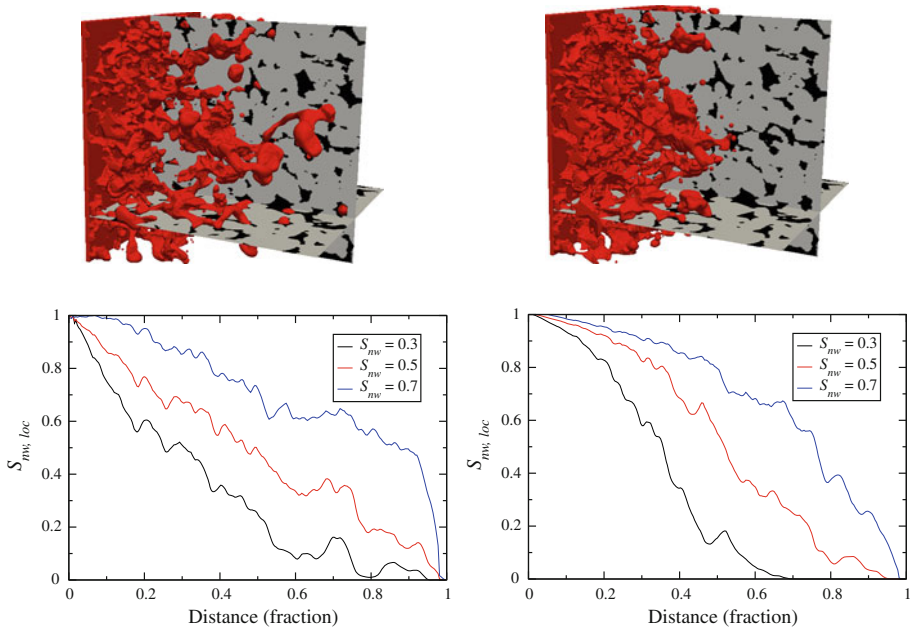

Fig. 3 Snapshots of the fluid configurations for primary drainage at global saturation $S_{\mathrm{nw}} \approx 0.3$ (*top*) with associated profiles of local saturations $S_{\mathrm{nw,loc}}$ (*bottom*) for two different flowrates in the Bentheimer sample. The nonwetting fluid is *red* and the pore space is *black*. For simplicity, we do not show the wetting fluid. The *left picture* shows a drainage process at $Ca = 1.0 \times 10^{-4}$, with $S_{\mathrm{nw}} \approx 0.3$ (corresponding to the *black* saturation profile), there is visible fingering ahead of the main front that has reached the outlet of the grid model. The *right picture* shows a drainage process at $Ca = 5.0 \times 10^{-6}$, with $S_{\mathrm{nw}} \approx 0.3$ (corresponding to the *black* saturation profile). This drainage simulation exhibits capillary fingering and the front is more compact

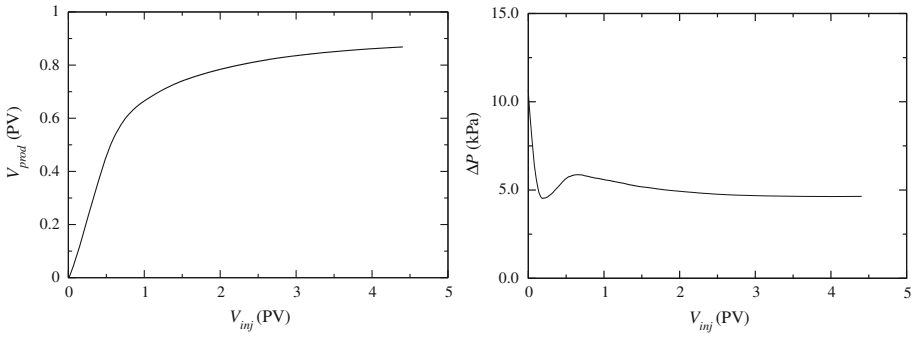

Fig. 4 Produced volume and pressure drop for drainage simulations in the Bentheimer sample with $Ca = 1.0 \times 10^{-4}$. The breakthrough of the nonwetting phase is not very distinct, and there is not a clear peak in the pressure profile at breakthrough

displacement similar to that of centrifuge setups which is commonly used for that purpose. However, such a displacement behaviour does not resemble the flooding process in the field.

A more profound observation from our results is that the derived $k_{\mathrm{r,nw}}$ is much larger than the steady-state data, especially at high S_{w}. This discrepancy can be partly explained by the high flowrate ($Ca = 1.0 \times 10^{-4}$) that for the initial displacement makes the capillary forces

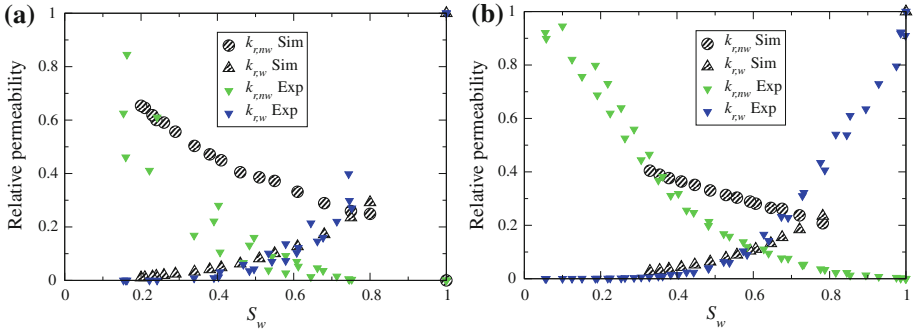

Fig. 5 Relative permeabilities for the drainage simulation derived from JBN post-processing. **a** is for the Bentheimer sample and **b** for the Berea sample. The simulations are compared to steady-state drainage data for the respective rocktypes with similar absolute permeability

negligible. It is well established that relative permeability curves will tend towards straight lines for high capillary numbers and near miscible flow as mentioned earlier in Sect. 3.

However, the capillary forces are not totally negligible in our simulations. Hence, the over-prediction of $k_{\mathrm{r,nw}}$ compared to steady-state data can not be explained by differences in flowrates alone. This is clearly shown by the fact that the wetting phase $k_{\mathrm{r,w}}$ curve is much closer to the steady-state one. For the invading phase, it is obvious that transient viscous instabilities determine the flow conditions and the fluid configurations. These transient instabilities and the local potentials linked to the movement of interfaces will add extra driving forces to the flow and consequently enhance the flux of the invading fluid. As a consequence, the relative permeability for unsteady-state needs to take dynamic effects into consideration and is not only a function of the saturation (Joekar-Niasar and Hassanizadeh 2011).

Closer to the saturation endpoint, it is assumed that most of the transients have vanished, and the unsteady-state data are closer to the steady-state ones. The fluid configurations for the high and low Ca-cases will become more similar as can be seen partly from the late saturation profiles in Fig. 3. It is also evident that the last points of the $k_{\mathrm{r,nw}}$ curve in Fig. 5 agree with the steady-state ones. Thus, it is obvious that the unsteady-state measurements of relative permeability have fundamental differences compared to steady-state when transient effects are present.

The JBN-derived $k_{\mathrm{r,w}}$ compares reasonably well with the steady-state data. The wetting phase relative permeability is largely unaffected by the viscous transients because the wetting phase flows in films where the only driving force is the viscous pressure gradient. Hence, the flowrate response can be determined from Darcy's law in Eq. 10.

4.3 Unsteady-state Imbibition

Next, we inject wetting fluid into the samples to displace nonwetting fluid—*imbibition*. The invading wetting fronts are depicted in Fig. 6, and leave ganglia of trapped nonwetting fluid behind. For the high flowrate $Ca = 5.0 \times 10^{-5}$, we observe a piston-like displacement, while the displacement front for $Ca = 5.0 \times 10^{-6}$ is not that well-defined. The cause of the difference is a relative increase in the transport of wetting fluid through films along the wetted surfaces for lower flowrates (Idowu and Blunt 2010). It is also evident from our simulations that much of the displacement at $Ca = 5.0 \times 10^{-6}$ is spontaneous and governed by capillary forces. Hence, as stated in Sect. 4.2, the assumption on which the JBN analysis is based is

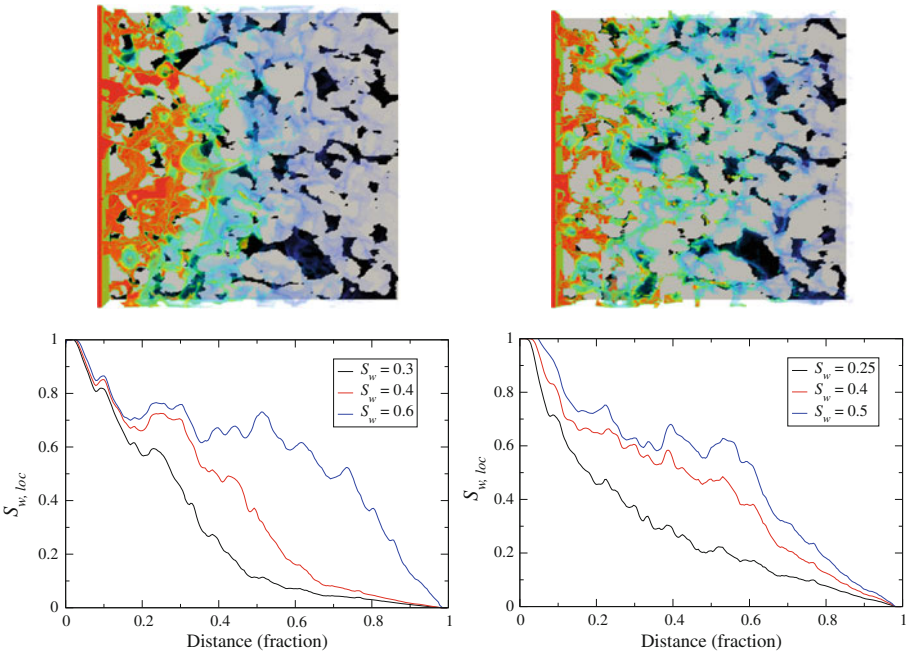

Fig. 6 Snapshots of the fluid configurations for imbibition at global saturation $S_{\mathrm{w}} = 0.4$ (*top*) with associated local saturation profiles (*bottom*) for two different flowrates in the Bentheimer sample. The wetting fluid is displayed with a colour palette with *red* as the largest concentration towards *blue* as the least concentration. The pore space is *black*. The *left picture* shows an imbibition process at $Ca \approx 5.0 \times 10^{-5}$. The *right picture* shows an imbibition process at $Ca \approx 5.0 \times 10^{-6}$

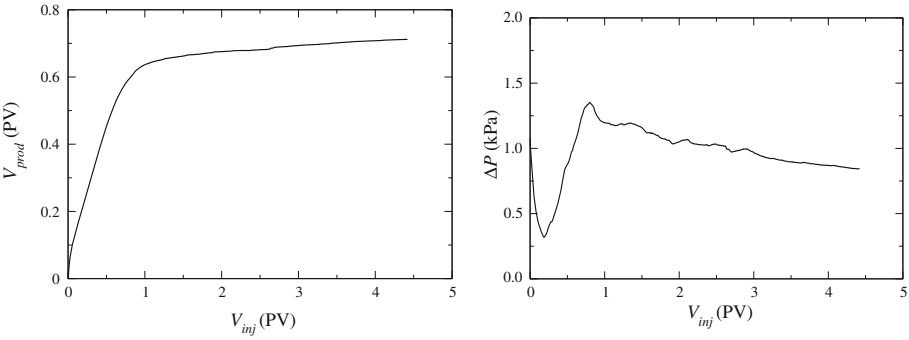

Fig. 7 The *left figure* shows the produced volume as a function of injected fluid in PV during imbibition in the Bentheimer sample at $Ca = 5.0 \times 10^{-5}$. The *right figure* shows the pressure drop over the model for the same capillary number

violated, and we are not able to extract relative permeability data for capillary regimes of $Ca < 10^{-5}$.

Figure 7 shows the nonwetting phase production and corresponding pressure drop as a function of injected PV. Compared to the drainage results, we observe a sharper change in the production profile and a well-defined peak in the global pressure drop. Before the peak there

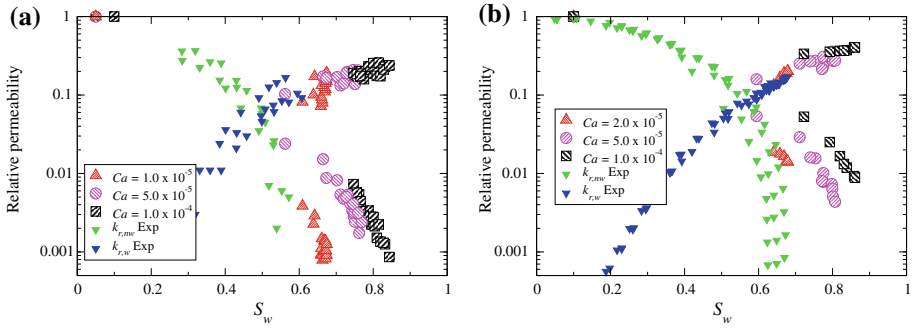

Fig. 8 Plots of relative permeability for imbibition at different Ca. **a** Shows result for the Bentheimer sample while **b** is for the Berea sample. The results are compared to steady-state imbibition experiments

is an almost linear increase in pressure. This corresponds to a linear increase in cumulative nonwetting phase production before breakthrough.

Figure 7 also shows that the effluent profile has the appearance of a piston-like displacement with little production after breakthrough, as expected for water-wet systems. This limits the applicability of the JBN method to derive relative permeability curves since most of the displacement is disguised. This is demonstrated in Fig. 8 which shows that relative permeabilities can only be derived for a limited saturation range, which is a limitation of unsteady-state techniques in general.

Changes in the flowrate have significant effects on the residual nonwetting phase saturation, as shown in Fig. 8. In an experimental setting this is categorized as a "bump rate", and is used to determine residual saturations. In our simulations, we also observe clear rate effects in the nonwetting phase relative permeability curves. For the wetting phase, the bump rate only extends the saturation range, but the relative permeability data follow the same curve path.

4.4 Methodology Comparison

In the two previous sections, we have compared our *unsteady-state* simulated relative permeability data with the available *steady-state* data and pointed out similarities and discrepancies. A pertinent question to ask is: Under what conditions are the results of the two methods comparable?

Several studies in the literature report that there often are agreements between relative permeabilities obtained from either technique within the uncertainties of experimental measurements (Dullien 1992). However, others report systematic discrepancies (e.g. Craig 1971; Eleri et al. 1995) especially for certain rock types, flow regimes and wetting conditions.

In general, the steady-state technique is most representative for the situation deep inside a reservoir, where boundary effects are negligible. In such a flow situation, the distribution of phases will be uniform and capillary equilibrium prevail without transient effects (Honarpour et al. 1986). In addition, relative permeabilities can be measured directly using steady-state techniques. Hence, it is less dependent upon assumptions compared to the indirect calculations of relative permeability curves from the unsteady-state method (Mohanty and Miller 1991).

In Fig. 8, we observe that the imbibition relative permeability for the wetting phase, $k_{\mathrm{r,w}}$, shares the same curve path as the steady-state experimental data, while the $k_{\mathrm{r,nw}}$ tends to be

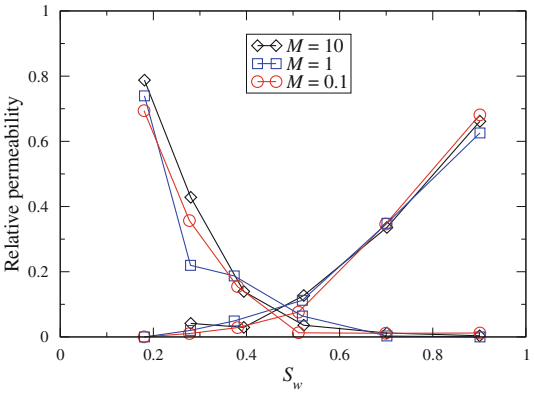

Fig. 9 Relative permeability for steady-state drainage in the Bentheimer sample with various viscosity contrasts M for $Ca = 2.0 \times 10^{-6}$

comparable for $Ca = 1.0 \times 10^{-5}$ for the Bentheimer sample and $Ca = 2.0 \times 10^{-5}$ for the Berea sample. It has been stated previously that the steady-state experiments were carried out at $Ca \approx 2.0 \times 10^{-6}$, but that at this low Ca, JBN assumptions are violated. Hence, we can not compute relative permeabilities using the JBN method. If it was possible to calculate relative permeabilities at this low capillary number, it is probable that the $k_{\mathrm{r,nw}}$ following the predicted trend would match the steady-state data better.

The drainage relative permeabilities for the wetting phase shown in Fig. 5 also show a good match with the steady experimental data. However, our simulation results show that the $k_{\mathrm{r,nw}}$ obtained from the unsteady-state simulations are fundamentally different from the steady-state results. Transient effects and nonuniform fluid configurations affect the estimated relative permeabilities. Similar results have been presented in previous studies, e.g. in Joekar-Niasar and Hassanizadeh (2011).

4.5 Viscosity Contrast

We have focused on the special case of fluids with equal viscosity in this study, but this is indeed only valid for a limited number of applications. To check the dynamic effects of various viscosity contrasts, we have run both steady-state and unsteady-state to directly compare viscosity contrasts with the equal viscosity setup. In this context, we define viscosity contrast as

$$M = \frac{\mu_{\mathrm{nw}}}{\mu_{\mathrm{w}}}. \tag{16}$$

From previous studies (Dullien 1992), it is found that for completely capillary-dominated displacements, i.e. low Ca, the viscous properties of the fluids have little impact on the relative permeabilities. The explanation for this is that the fluid configurations will be determined by capillary effects alone. If viscous forces and apparent viscous coupling have to be taken into consideration, the picture changes.

In Fig. 9, steady-state drainage simulations with $Ca = 2.0 \times 10^{-6}$ with various viscosity ratios are displayed. The relative permeabilities are calculated from Eq. 10, but with the effective viscosity $\mu = (1 - S_{\mathrm{w}})\mu_{\mathrm{nw}} + S_{\mathrm{w}}\mu_{\mathrm{w}}$ rather than the individual phase viscosities. Within the expected uncertainty of these simulations, the results are similar, suggesting that the viscosity ratios have no effect on the relative permeabilities. However, close to the end-points, we observe a slight systematic shift in the different $k_{\mathrm{r,nw}}$.

Viscosity contrasts can have impacts on the invasion patterns for unsteady-state setups, but for imbibition processes a small viscosity contrast has little effect on the qualitative saturation

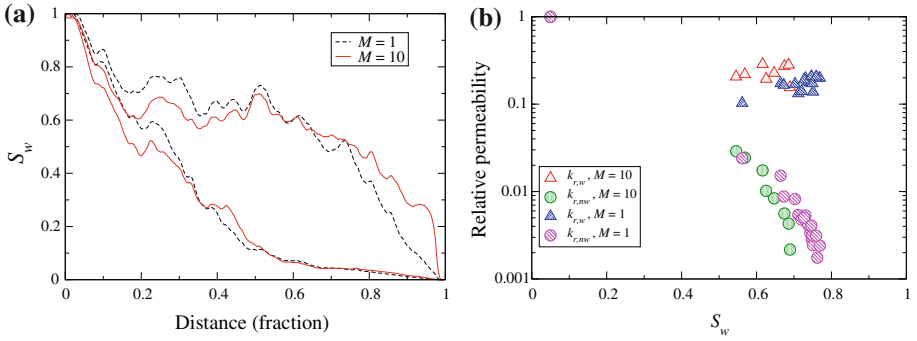

Fig. 10 The *left figure* shows saturation profiles for imbibition with viscosity contrast $M = 10$ and $M = 1$ with $Ca = 5.0 \times 10^{-5}$. The corresponding relative permeabilities are shown in the *right figure*

profile as shown in Fig. 10. However, we observe a higher residual nonwetting saturation for $M = 10$ compared to the equal viscosity case. This is categorized as an unfavourable viscosity ratio.

5 Conclusion

We have applied a LB method to systematically obtain relative permeability functions from digitized microstructure images of Bentheimer and Berea sandstone under water-wet conditions. We demonstrate that the LB method can reproduce drainage and imbibition relative permeabilities obtained by different experimental measurement methods and imposed flow conditions.

All computed results are compared to available steady-state experimental data. The qualitative and quantitative behavior of the LB simulations are fully comparable to the experimental data for steady-state setups, and this provides as a good benchmark for further extensions of the simulations.

We find that the JBN-derived nonwetting phase relative permeability for unsteady-state drainage simulations is over-predicted compared to the steady-state results. This is due to transient viscous instabilities that violate the assumptions of the generalized Darcy's law for two-phase flow. From this, we conclude that transient effects create fundamental differences between steady and unsteady-state measurements of relative permeabilities for drainage. The wetting, defending fluid is less affected and is comparable to the experimental steady-state data.

Unsteady-state imbibition simulations show the expected qualitative behaviour for both wetting and nonwetting fluids. We demonstrate that for unsteady-state displacements, residual saturations depend strongly on the capillary number.

Finally, we have discussed the dynamic effects of viscosity contrasts and how these affect the measured and calculated relative permeabilities from steady and unsteady-state simulations. We observe that the viscosity contrasts have little impact on the mid saturation range of the relative permeabilities, but may affect the end-point properties to a certain degree at low Ca.

The results obtained will eventually bring this study to be a part of a larger study that will systematically evaluate the capability of the LB method to predict multiphase flow functions for a wide range of fluid properties. Further, this will be applied towards geological

sequestration of CO_2. So far, the results are encouraging, and the LB method has shown predictive capabilities and the ability to account for viscous effects.

Acknowledgments We thank Numerical Rocks AS for granting permission to publish this article. A significant amount of computing time was granted by NOTUR, and part of the financing has been through the CLIMIT program: Project 203175 "Pore scale numerical analysis for geological sequestration of CO_2".

References

Ahrenholz, B., Tölke, J., Lehmann, P., Peters, A., Kaestner, A., Krafczyk, M., Durner, W.: Prediction of capillary hysteresis in a porous material using lattice-Boltzmann methods and comparison to experimental data and a morphological pore network model. Adv. Water Resour. **31**, 1151–1173 (2008)

Arns, C.H., Knackstedt, M.A., Pinczewski, V., Garboczi, E.J.: Computation of linear elastic properties from microtomographic images: methodology and agreement between theory and experiments. Geophysics **67**, 1396–1405 (2002)

Avraam, D.G., Payatakes, A.C.: Flow mechanisms, relative permeability, and coupling effects in steady-state two-phase flow through porous media. The case of strong wettability. Ind. Eng. Chem. Res. **38**, 778–786 (1999)

Badalassi, V., Ceniceros, H., Banerjee, S.: Computation of multiphase systems with phase field models. J. Comput. Phys. **190**, 371–397 (2003)

Bardon, C., Longeron, D.G.: Influence of very low interfacial tensions on relative permeability. SPE J. **20**, 391–401 (1980)

Bhatnagar, P.L., Gross, E.P., Krook, M.: A model for collision processes in gases. 1. Small amplitude processes in charges and neutral one-component systems. Phys. Rev. **94**, 511–525 (1954)

Craig, F.F.: The Reservoir Engineering Aspects of Waterflooding. Society of Petroleum Engineers of AIME, New York (1971)

d'Humières, D., Ginzburg, I., Krafczyk, M., Lallemand, P., Li-Shi, L.: Multiple-relaxation-time lattice Boltzmann models in three dimensions. Philos. Trans. R. Soc. Lond. A **360**, 437–451 (2002)

Dullien, F.A.L.: Porous Media: Fluid Transport and Pore Structure. 2nd edn. Academic Press, New York (1992)

Eleri, O.O., Graue, A., Skauge, A.: Steady-state and unsteady-state two-phase relative permeability hysteresis and measurements of three-phase relative permeabilities using imaging techniques. Paper SPE 30764, presented at the annual SPE conference and exhibition, Dallas, TX, USA (1995)

Gunstensen, A.K., Rothman, D.H., Zaleski, S., Zanetti, G.: Lattice Boltzmann model of immiscible fluids. Phys. Rev. A **43**, 4320–4327 (1991)

Honarpour, M., Koederitz, L., Harvey, A.H.: Relative Permeabilities for Petroleum Reservoirs. CRC Press, Boca Raton (1986)

Idowu, N.A., Blunt, M.J.: Pore-Scale modelling of rate effects in waterflooding. Transp. Porous Med. **83**, 151–169 (2010)

Inamuro, T., Ogata, T., Tajima, S., Konishi, N.: A lattice Boltzmann method for incompressible two-phase flow with large density differences. J. Comput. Phys. **155**, 96–127 (2004)

Jiang, Z., Wu, K., Couples, G., van Dijke, M.I.J., Sorbie, K.S., Ma, J.: Efficient extraction of networks from three-dimensional porous media. Water Resour. Res. **43**, W12S03 (2007)

Jin, G., Patzek, T.W., Silin, D.B.: Direct prediction of the absolute permeability of unconsolidated and consolidated reservoir rocks. Paper SPE 90084, presented at the annual SPE conference and exhibition, Houston, TX, 26–29 September 2004

Joekar-Niasar, V., Hassanizadeh, S.M.: Specific interfacial area: the missing state variable in two-phase flow equations?. Water Resour. Res. **47**, W05513 (2011)

Johnson, E.F., Bossler, D.D., Naumann, V.O.: Calculation of relative permeability from displacement experiments. Trans. AIME **216**, 370 (1959)

Knackstedt, M.A., Arns, C.H., Limaye, A., Sakellariou, A., Senden, T.J., Sheppard, A.P., Sok, R.M., Pinczewski, W.V.: Digital Core Laboratory: properties of reservoir core derived from 3D images. SPE paper 87009, Kuala Lumpur, Malaysia (2004)

Lallemand, P., Luo, L.A.: Theory of the lattice Boltzmann method: dispersion, isotropy, Galilean invariance and stability. Phys. Rev. E **61**, 6546 (2000)

Latva-Kokko, M., Rothmann, D.H.: Diffusion properties of gradient-based lattice Boltzmann models of immiscible fluids. Phys. Rev. E **71**, 056702 (2005)

Lindquist, W.B., Lee, S.M., Coker, D., Jones, K., Spanne, P.: Medial axis analysis of void structure in three-dimensional tomographic images of porous media. J. Geophys. Res. **101**, 8297 (1996)

Marle, C.M.: Multiphase Flow in Porous Media. Editions Technip, Paris (1981)
Martys, N., Chen, H.: Simulation of multicomponent fluids in complex three-dimensional geometries by the lattice-Boltzmann method. Phys. Rev. E **53**, 743–750 (1996)
Mohanty, K.K., Miller, A.E.: Factors influencing unsteady relative permeability of a mixed-wet reservoir rock. SPE Form. Eval. **6**, 349–358 (1991)
Oak, M.J., Baker, L.E., Thomas, D.C.: Three-phase relative permeability of Berea sandstone. JPT August 1990, 1054 (1990)
Øren, P.E., Bakke, S.: Process based reconstruction of sandstones and prediction of transport properties. Transp. Porous Media **46**, 311–314 (2002)
Øren, P.E., Bakke, S.: Reconstruction of Berea sandstone and pore scale modeling of wettability effects. J. Pet. Sci. Eng. **39**, 177–199 (2003)
Øren, P.E., Bakke, S., Arntzen, O.J.: Extending Predictive Capabilities to Network Models. SPE J. **3**, 324–336 (1998)
Øren, P.E., Bakke, S., Rueslåtten, H.G.: Digital core laboratory: rock and flow properties derived from computer generated rocks. In: Proceedings of International Symposium of the Society of Core Analysts, Trondheim, Norway (2006)
Pan, C., Hilpert, M., Miller, C.T.: Lattice-Boltzmann simulation of two-phase flow in porous media. Water Resour. Res. **40**, W01501 (2004)
Pan, C., Luo, L.-S., Miller, C.T.: An evaluation of lattice Boltzmann schemes for porous medium flow simulations. Comput. Fluids **35**, 898–909 (2006)
Ramstad, T., Hansen, A.: Cluster evolution in steady-state two-phase flow in porous media. Phys. Rev. E **73**, 026306 (2006)
Ramstad, T., Øren, P.-E., Bakke, S.: Simulation of two phase flow in reservoir rocks using a lattice Boltzmann method. SPE J. **15**(4), 917–927 (2010)
Rothmann, D.H., Zaleski, S.: Lattice-Gas Cellular Automata. Cambridge University Press, Cambridge (1997)
Schaap, M.G., Porter, M.L., Christensen, B., Wildenschild, D.: Comparison of pressure-saturation characteristics derived from computed tomography and lattice Boltzmann simulations. Water Resour. Res. **43**, W12S06 (2007)
Shan, X., Chen, H.: Lattice Boltzmann model for simulating flows with multiple phases and components. Phys. Rev. E **47**, 1815–1819 (1993)
Succi, S.: The Lattice Boltzmann Equation. Clarendon Press, Oxford (2001)
Succi, S., Foti, E., Higuera, F.: Three dimensional flows in complex geometries with the lattice Boltzmann method. Europhys. Lett. **10**, 433 (1989)
Sukop, M.C., Thorne, D.T.: Lattice Boltzmann Modeling. An Introduction for Geoscientists and Engineers. Springer, Berlin (2006)
Sussman, M., Smereka, P., Osher, S.: A level set approach for computing solutions to incompressible two-phase flows. J. Comput. Phys. **114**, 146–159 (1994)
Swift, M.R., Osborn, W.R., Yoemans, J.M.: Lattice Boltzmann simulations of non-ideal fluids. Phys. Rev. Lett. **75**, 830 (1995)
Tryggvason, G., Sussman, M., Hussaini, M.Y.: Immersed boundary methods for fluid interfaces. In: Prosperetti, A., Tryggvasson, G. (eds.) Computational Methods for Multiphase Flow, pp. 37–78. Cambridge University Press, Cambridge (2007)
Valvatne, P.H., Blunt, M.: Predictive pore-scale modeling of two-phase flow in mixed wet media. Water Resour. Res. **40**, 1–21 (2004)